Accepted Manuscript - Journalof Hydrology https://doi.org/10.1016/j.jhydrol.2018.09.067

Combining COSMO-SkyMed satellites data and numerical modeling for the dynamic management of artificial recharge basins

Marco Masetti[a,*], Simone Pettinato[b], Son V. Nghiem[c], Simonetta Paloscia[b], Daniele Pedretti[d], Emanuele Santi[b]

[a] Dipartimento di Scienze della Terra "A. Desio", Università degli Studi di Milano, Milan, Italy [b] Institute of Applied Physics (IFAC), National Research Council of Italy, Florence, Italy [c] Jet Propulsion Laboratory, California Institute of Technology, Pasadena, CA, USA [d] Geological Survey of Finland (GTK), Espoo, Finland

A B S T R A C T

Many urbanized areas in the world are using artificial recharge basins (ARB) as an efficient solution to maintain adequate groundwater recharge while coping with flooding problems. The effective management of these basins to adequately maintain their functionality over mid-to-long term requires a suitable monitoring network. Here, we explored the use of a temporal satellite analysis to closely evaluate the efficiency of the ARB in terms of infiltration capacity, depending on hydraulic conditions of the topsoil transitioning from unclogged to clogged conditions in the ARB.

COSMO-SkyMed synthetic aperture radar (SAR) images were integrated with ground data and numerical modeling to advance the capability for monitoring low water levels and flooded areas within the ARB. The understanding of biofilm development and effects was achieved by identifying anomalous drawdown phases, by constraining ponding boundary conditions in the numerical model, and by estimating subsequent infiltration rate changes under progressive clogging.

With appropriate meteorological conditions (consecutive rainfall events separated by few dry days), the biofilm could develop rapidly and cover large surfaces (e.g., 22 ha) in about two months. During this process, the hydraulic conductivity of the basin surface could decrease by more than three orders of magnitude, completely altering the relationship with the local groundwater regime. Quantitative estimation of the evolution of the infiltration rate provides crucial insights about the overall recharge behavior of ARBs to make reliable economical plans in both the design and monitoring phase.

Keywords:Groundwater, Artificial recharge basin, Infiltration, Remote sensing, SAR, Clogging

1. Introduction

Artificial recharge basins (ARBs) are hydraulic engineering facilities adopted for a variety of purposes, including managed aquifer recharge (MAR) (e.g. Martin, 2013). ARBs work by diverting surficial water intentionally into the basins, to tackle water shortage problems (Buhyain, 2015). Moreover, ARBs are used to reduce storm water floors, while forcing part of surficial water to infiltrate into the subsurface through the ARBs topsoil (Kattan et al., 2010).

The correct use of ARBs requires an adequate and frequent monitoring of water levels within the ARBs. This effort can be complicated by several factors. For instance, the installation of in-situ instrumentation can be costly and difficult, and the data reading may be susceptible to failures resulting in incomplete records (e.g. Masetti et al., 2016). Moreover, the irregular geometry of the surface may let water accumulate preferentially in some parts of the ARBs, leaving other areas partially inundated or even completely empty. Such irregularity of the ground surface was observed during a field campaign in July 2015 (Masetti et al., 2015) on a large ARB located in the Po Plain in northern Italy, an area frequently subject to flooding due to the extensive urbanization. Given that it is virtually impossible to install water level sensors in all possible portions within the ARB, manual measurements of water levels within the ARB would be needed, resulting in potentially high operational costs for ARB monitoring.

Another complication is the clogging formation, such as biofilm on the ARB bottom surface, which sporadically masks the ground surface. The biofilm cover may lead to differential infiltration of water in specific sectors of the ARB (e.g. Pedretti et al., 2012a) or to an extensive impermeable surface across the entire ARB (Martin, 2013). This process is rather common in all managed aquifer recharge facilities (Racz et al., 2012) and plays a crucial role in maintenance cost-and system performance (Houle et al., 2013).

Optical and microwave remote sensing techniques have already been successfully used to observe terrestrial water with applications related to river discharges and runoffs (Brakenridge et al., 2005; Brakenridge et al., 2007), groundwater recharge (Khalaf and Donoghue, 2012; Coelho et al., 2017), wetlands, (Nghiem et al., 2017), global health (United Nations, 2017), flood hazards (DFO, Dartmouth Flood Observatory, 2016), water resources management (Alsdorf et al., 2007; Nghiem et al., 2012), and snow cover (Pettinato et al., 2013; Pettinato and Santi, 2014). For MAR involving infiltration basins, applications are scarce. Pedretti et al. (2011, 2012b) showed that satellite photographic images could be combined to ground measurements from double-ring infiltrometers to quantify the infiltration capacity of the ARBs ground surface before and after flooding events generating clogging. While this approach is a useful and promising tool to improve the design and management of these facilities, it was tested on a static pilot ARB area in absence of flooding water. However, operational ARBs are dynamic systems with a short time scale of flooding-emptying basin cycles (Masetti et al., 2016). In this case, an extensive series of images collected at high resolutions in time and in space over the same area are required to study the dynamic variability of flooding events in the basins. The problem of satellite optical images is that they are significantly affected by clouds and floating vegetation on the water surface (Fig. 1, inset in the right panel), which could partially or completely limit their use to monitor the water covered area in the basin (Ran and Lu, 2012). Moreover, water turbidity and suspended sediments may further complicate the spectral characteristics for water remote sensing.

Active microwave sensors, such as synthetic aperture radar (SAR), are very effective tools to detect the presence of water in various landscape conditions including open surfaces, vegetated agricultural lands, and urban areas, regardless of cloud cover and absence of solar illumination (Paloscia et al., 2008; Paloscia and Santi, 2012). Compared to other land surface types, water surface typically has very low radar backscatter, especially at large incidence angles, showing different polarization signatures depending on wind speed and wind direction (Grieco et al., 2015; Li and Lehner, 2014; Nghiem et al., 1997, 2004). This important property can be used to identify inland water bodies from other surface targets. Various applications of SAR in hydrological studies have been reported in the literature (e.g., Santoro and Wegmüller, 2014; Bartsch et al., 2012; Hostache et al., 2009; Pulvirenti et al., 2014; Xie et al., 2016). Details on the methods used to infer information

about water presence on soil surface and land use classification from satellite images, including threshold and change detection methods or unsupervised and semi-automated solutions, have been reported elsewhere (e.g., Santoro and Wegmüller, 2014; Pradhan et al., 2016; Pulvirenti et al., 2014; Paloscia et al., 2008; Paloscia and Santi, 2012; Pettinato et al., 2013; Pettinato and Santi, 2014).

This paper presents a novel framework, which combines SAR-based observations from the COSMO-SkyMed (CSK) satellites and numerical modeling, to support the management of large-scale ARBs by monitoring and predicting the dynamic change in ARB hydraulic behavior. The CSK system is a space-borne, four-satellite constellation, which is fully operational since 2011. CSK satellites are equipped with SAR sensors that operate at X-band in sun-synchronous orbits (Coletta et al., 2008; Grimani et al., 2016). The CSK SAR constellation enables much more frequent revisits to a specific location compared to the SAR coverage from a single-satellite mission. Different applications on the use of CSK for detecting waterline changes in intertidal area (Ding et al., 2015), and flooding areas boundaries in urban and agricultural areas (Pulvirenti et al., 2016; Boni et al., 2016) were published.

The goal of this analysis is to evaluate the capability of CSK SARs as a quantitative tool to support decision-making processes regarding MAR activities using ARBs. As a case study, we focus on the Po Plain ARB, where continuous measurements of local rainfall and aquifer head and a calibrated and validated numerical flow model are available to obtain quantitative estimates of transient changes in hydraulic properties of the ARB during the MAR activities (Masetti et al., 2016). Using these data and tools, our specific objectives are: (1) to explore any link between remote sensing information from CSK satellites and existing ground measurement from the targeted ARB to assess the impact on the local aquifer recharge, and (2) to explore the use of transient satellite analysis to evaluate the efficiency of the ARB in terms of topsoil infiltration capacity, particularly on the hydraulic conditions of the topsoil transitioning from unclogged to clogged conditions in the ARB.

In addressing the above goals, we explicitly note that the originality of the results to be presented in this paper includes: (1) use of the temporal dimension with frequent revisit by taking advantage of the CSK system as a constellation of SARs allowing the capability to resolve the short time scale involved in the hydrogeological processes occurred in the ARB, (2) establishing the relationship between satellite SAR observations with the ARB hydrological processes by using a composite of in-situ and surface observations together with modeling results, and (3) quantitative demonstration that the CSK constellation has sufficient capability for application to evaluate ARB efficiency and the effect on groundwater recharge.

2. Material and methods

2.1. Site overview

The analyzed site, of about 22 ha, is among the most extended ARBs in Italy. It is located about 40 km north-west of Milan (Fig. 1), in the central Po Plain in Northern Italy. A number of these facilities are currently active in this densely populated area. The area suffers from several flooding events that require the construction of multiple hydraulic facilities to cope with the related risks. Nevertheless, these facilities should also need to ensure the effective infiltration of stormwater to maintain adequate groundwater recharge in the area where about 5 million people are 100% dependent on groundwater for drinking water supply.

The ARB has a maximum depth of 4 m and is located in a flat area close to a series of morphological fluvial terraces due to the Ticino River, located to the west, which acts as a gaining stream causing a local groundwater flow direction from NE to SW (Fig. 2). The average annual rainfall depth is about 900 mm/y and the average groundwater depth is between 30 and 34 m from the natural land surface. In the area, the aquifer is unconfined, relatively homogeneous and highly permeable, and mainly made up of gravel and sands deposit of fluvial origin. The aquifer transmissivity is estimated at about 10^{-2} m^2/s (Masetti et al., 2016). The presence of discontinuous clay layers starts from 50 m below the natural land surface (Fig. 2).

The ARB was activated in 2001 to mitigate the flood risk due to local Arno Creek fluvial regime and to contribute to aquifer recharge. The Arno Creek does not have any base flow and conveys water to the basins in rainfall periods only. The site has two pre-sedimentation basins (V1 and V2), which alternatively receive the first flooding waters from the Arno Creek, and a main infiltration basin (i.e. the actual ARB, V3), where surface water is infiltrated into the ground (Fig. 1).

The ARB topsoil became clogged and practically impervious in 2006. After 5years of legal issues, clogging was removed only in 2011, and a new 5-cm thick gravel layer was deposited on top of the natural unclogged ground. The cleaning operations showed that the clogging was mainly due to biological activity with a limited presence of fine sediments on the basin surface. The ARB appeared to suffer a new persistent ponding condition in 2014 caused by clogging primarily due to biological activities (Masetti et al., 2016). Detailed ground information on timing and ponding dynamics were not available once again, exerting an urgent demand on the important analysis of archival satellite remote sensing data acquired over the ARB.

2.2. Ground monitoring and previous numerical modeling

A monitoring plan was developed in 2011 to study effects of the infiltration basin on groundwater quantity and quality in the area, to assess mutual interactions between surficial stored water and groundwater, and to estimate the transient infiltration rate through the bottom of the basin. The vadose zone and the aquifer underneath the ARB have been investigated with in-situ permeability tests and aquifer head measurements recorded hourly in two piezometers (PZ1 and PZ3 in Fig. 1); piezometers are located at a distance of about 50 m from the upgradient and downgradient basin boundaries, respectively. Groundwater head changes in the upgradient PZ1 are mostly affected by the natural recharge while head changes in downgradient PZ3 are influenced by both the natural recharge and the artificial recharge imposed by the ARB. Rainfall data were also recorded hourly at a local weather station, located about 1.5 km northward.

Using these observations, Masetti et al. (2016) presented experimental data showing that, before 2011, the natural recharge in the aquifer nearby the facility (i.e. recharge not directly affected by the ARB) was quite high, resulting in a short residence time of 36–48 h in the ~30 m-thick vadose zone. A calibrated groundwater flow model was then developed upon these observations to replicate the ARB effects on local recharge. The model showed that, under unclogged ARB conditions, local recharged volumes underneath the basin can be more than fifty times higher than the volumes associated with natural recharge. The numerical model estimated that the ARB could infiltrate more than 10^6 m^3 in a single flooding event that typically occurred 5 to 10 times each year. The same numerical model was extended and used in the analyses in this manuscript (ref. Section 3.2).

Masetti et al. (2016) highlighted that the geometrically irregular ARB ground surface induced the flooding water to flow preferentially towards specific areas of the basin. This aspect is relevant because of two factors: (1) it directly affects the estimation of water volumes actually existing in the system during a specific

flooding stage (and thus generating wrong estimation of the total water that can potentially recharge the aquifer); (2) the clustered presence of ponding water in the ARB tends to form clogging preferentially in specific areas of the ARB, thus generating heterogeneous reduction of the ARB infiltration capacity of the topsoil. The model by Masetti et al. (2016) is therefore calibrated and validated against ground observed measurements. In this work, we extend the use of this model as an exploratory tool, by using the CSK satellite information to impose the boundary conditions required to define the functioning stages of the SIB.

2.3. Satellite imaging methodology

2.3.1. Satellite SAR data

Seventy CSK SAR images were acquired by the Italian Spatial Agency (ASI) over a three-year period, between June 2012 and December 2014 (Supplementary Material). The multi-temporal SAR images enable us to study closely the evolution of the extension of the inundated area in this analysis.

The focus of images data processing was the V3 basin, serving as the actual infiltration basin. We did not consider in the analyses the sedimentation basins V1 and V2 because they do not exert any influence on groundwater recharge. This is because their bottom surfaces are impermeable and do not allow any infiltration; these basins are always full of water, except during the days of maintenance operations occurring about every two years.

The SAR data processing has been specifically performed for the study. The processing method is described by the satellite data provider (ASI, 2007) and by the official distributor (E-Geos, 2012). The processing parameters, including orbital parameters and calibration constants, were extracted from the ancillary data associated with each SAR image to radiometrically calibrate radar backscatter data and to accurately geocode the images with standard methods using the Shuttle Radar Topography Mission (SRTM) digital elevation model (Bamler, 1999).

2.3.2. Classification method

The complete detailed steps in the methodology for the classification of surface water include:

1. A multi-look filter with a 2 ×2 pixel window was applied to maintain a good spatial resolution in the SAR images in slant range view. After the geocoding procedure, the resultant pixel size is 10 m that is appropriate to identify surface water areas in the 22-ha ARB with sufficient details. The images were co-registered in a stack file to compare the multi-temporal CSK images pixel-by-pixel.
2. For all images, we obtained fully calibrated backscattering coefficient, σ_0, measured on the ARB which was typically above the noise equivalent sigma zero (NESZ) at about −22 dB (Torre et al., 2011).
3. We classified each pixel in each co-registered SAR image as “covered” or “not covered” by water, by means of the following change detection method. In each co-registered image, we initially identified the borders of the ARB in order to uniquely define the maximum ARB infiltration area that could be potentially covered during flooding stages (A). Three images (acquired on July 3rd, 5th, and 19th, 2012) were used for this purpose, all taken in summer when the ARB was completely empty, as verified by ground observations. The reference backscattering image of the empty ARB was generated after averaging over these three samples images.
4. Finally, for each existing co-registered image, we computed thedifference in pixel intensity between the selected image and the reference image. The presence of water was identified for each pixel when the difference in intensity was greater than 6 dB.

For the water classification, the backscatter threshold (6 dB) is quantitatively determined by the different backscatter intensity level of specular surfaces (i.e. calm water), which is significantly lower than backscatter intensity detected in the ARB when it is empty. The backscatter coefficient, in fact, in terms of mean values acquired on the water body of the ARB, ranges from −22 dB to −17 dB and this is also in line with previous studies (Ulaby et al., 1986; Pierdicca et al., 2009). On the other hand, the backscatter coefficient acquired on no-flooded area of the ARB is significantly higher (more than −12 dB, in terms of mean values). On the base of these statistics, in order to select the most appropriate threshold, the relative accuracy error, defined as the smallest common backscatter range between water body backscatter and the reference intensity image backscatter is computed and normalized to the total backscatter range (i.e. flooded and no-flooded backscatter) of each satellite image. Threshold from 3 to 6 dB is applied, retrieving a relative accuracy of 20–6%, respectively. Because of this reason, the 6 dB threshold is selected.

The ARB is surrounded by a high levee (~4.5 m) and tall trees (see far side of the ARB in the photograph inset in the top right panel of Fig. 1), which shield the ARB resulting in calm conditions. The calm and thus smooth water surface has low backscatter, which is less than −13 dB for calm conditions with wind speed < 2 m/s (i.e., below Force 2 in the Beaufort wind scale) at the upwind direction (Grieco et al., 2015) for the incidence angle of 26° (smallest incidence angles among all SAR images; see Table 1S).

The calm water surface backscatter decreases at larger incidence angles and can plummet to below the noise floor at the largest incidence angle of 45° in the range of incidence angles of the CSK SAR scenes used in this study (Table 1S). Moreover, floating vegetation in the ARB (see photograph inset in Fig. 1) effectively suppresses capillary waves on the water surface and thereby further lowering the backscatter.

2.3.3. Advantage of the CSK method

Regarding water detection methods by using high-resolution multispectral data, such as Landsat (Shi et al., 2017), we noted that, unfortunately, many Landsat images available in the selected time period were cloud-covered. CSK observations are not affected by clouds and are independent of solar illumination, thus allowing day/night observations. Moreover, CSK SAR data, with a spatial resolution of 10 m, which is higher than the one of Landsat (~30 m), and the frequent temporal coverage derived from the CSK constellation, play a significant role in meeting the requirement of water detection, particularly for the scale of the ARB and the multi-temporal revisit considered in this paper. No cloud-free contemporary acquisitions from Landsat were available in order to compare the water body area extension from CSK for the cases considered in this paper.

Considering other optical sensors, the Sentinel MultiSpectral Instrument (MSI) has a resolution of 10 m comparable to the CSK resolution at some bands; however, other bands (i.e. near infrared) have a slightly coarser resolution of 20 m (ESA, 2017a). In any case, MSI shows the same limitations of Landsat (i.e. all the optical sensors), being affected by clouds and darkness especially in winter.

Compared to other SAR systems, the CSK constellation has four SAR satellites, while RADARSAT-2 (CSA, 2017) and Sentinel-1A/1B have only one and two SAR satellites in each system, respectively (ESA, 2017b). Thus, the CSK constellation has a better temporal coverage to provide multiple repeated observations required to track surface water changes that can be linked to short-time-scale hydrological processes in the ARB. This can be noted from the list of available CSK images used in this work and showed in Table 1S.

2.3.4. Quantification of water area and macro-classes

Quantitatively, the area of ARB effectively covered by water (A_w) was computed as the number of pixels with detected presence of water multiplied by the pixel area. The same pixel classification method was applied to all images from the CSK SAR dataset to evaluate the temporal trends of the proportion (p) of infiltration area covered by water, expressed as a percentage as $p(t) = 100 \times A_w(t)/A$

where t is time.

With the computed percentage of water cover in the ARB, four macro-classes were defined as

- Class 1: p > 90% i.e. ARB almost entirely covered by water;
- Class 2: 50% < p < 90%;
- Class 3: 0% < p < 50%;
- Class 4: p =0%, i.e. no water in the ARB.

As described in detail in the next section, we use this information to: (a) provide a qualitative assessment of clogging conditions and the relationship with rainfall events, (b) expand the numerical model possibilities to obtain quantitative information on the rate of bio-clogging formation and on the related changes in hydraulic conductivity of ARB topsoil, constrain the boundary conditions of the numerical model and predict the hydraulic response of the aquifer at the two piezometers.

An example of original (i.e., non-classified) CSK image and the corresponding classified image is presented in Fig. 3. In the top panel, we show a series of selected original images in gray scales that are proportional to the normalized backscatter power (in dB) of the radar signal measured by the satellite SARs and related to the reference image. The red line identifies the ARB boundary. In the bottom panel, we show the resulting binary classified image, where black pixels within the red line represents the part of the pond actually flooded by a storm water event associated with the overflow of the Arno creek. V1 and V2 were excluded from this analysis as noted earlier, and were blackened out in bottom panel.

3. Hydrological applications

3.1. Correlation between image classes and ground measurements

The satellite-estimated time evolution of the proportion of ARB covered by water from May 2012 to December 2014 is shown in Fig. 4. From the figure, the infiltration basin was almost entirely flooded and then completely emptied several times during the period 2012–2013. Afterwards, the ARB was persistently filled by water in 2014. This analysis is consistent with the behavior of the ARB visually observed from ground, which qualitatively matches the expected behavior of clogging in the site. Before 2014, ponding water in the system was discontinuous and associated uniquely to clustered rainfall events (e.g. Masetti et al., 2016). During this period, clogging was not yet forming sufficiently to limit the overall infiltration capacity of the basin after the previous topsoil maintenance (occurred in 2011). Evaporation cannot be responsible for the total water losses from the basin. In fact, evaporation losses are generally low in highly permeable systems when the basin has limited storage capacity, (e.g. Bouwer, 2002). Around May 2013, the ARB was found to show longer time periods with $p > 90\%$, suggesting that the ARB was mostly covered by water, while after 2013 the water ponding was continuously persistent in the infiltration basin (as shown in Fig. 4).

From the observed results, the proportion of topsoil covered by water only slightly declined in the system during the June-September 2014 windows, corresponding to usually hot summer periods in Northern Italy. The slight decline (less than 5% of the total surface, see Fig. 4) confirms that evaporation, expected to reach the maximum rate during summer, is only a minor component of the system water balance in this ARB.

The analysis of satellite images provides a first qualitative assessment of the transition from unclogged conditions to fully clogged conditions in the analyzed ARB. In particular, four stages can be identified (Fig. 4):

1. In 2012, a large part of the ARB was actively infiltrating water, limiting water presence in the basin both in space and time ($p \approx 0$), as a consequence of the removal of the clogging layer from the ARB surface in 2011 (pre-clogging).
2. In the first half of 2013, a transient increase in ponding water persistency in the system was observed, suggesting the initial impact of clogging in the ARB (50 < p < 90%) (temporary clogging).
3. In the second half of 2013, a prolonged dry period caused biofilm biodegradation which partially restored the good initial infiltration conditions ($p \approx 0$) (self declogging)
4. In 2014, clogging started affecting more heavily and permanently the topsoil, which became fully clogged in the 2014 ($p = 1$) (permanent clogging).

To evaluate the quantitative use of image classification for MAR applications, in particular to quantify the impact of the ARB on recharge, we compare the relationship between infilling status of the ARB estimated from the images and ground measurements referring to groundwater head values in response to rainfall events observed in the site during the period 2012–2014. The groundwater head of piezometer Pz3, located downgradient of the ARB, is sensitive to both natural and artificial recharge events when the ARB is not clogged and to only natural recharge when the ARB is clogged. Consistent to very high infiltration rates and low evaporation in the site, groundwater head responses in PZ3 are highly correlated with the detected presence of water in ARB.

This phenomenon is indeed supported by the dataset from the analyzed ARB. Fig. 5 reports the depth to groundwater vs rainfall height overlapped by the estimated macro-classes using satellite SAR data. We divided the time series in the three years covered by satellite monitoring, relating data to the clogging status of the ARB listed above. In this quantitative analysis, we analyzed the fluctuation in groundwater heads (Δh) from a basal reference head value.

In the 2012 time window (Fig. 5 – top panel), the head response of the piezometer was quite short, suggesting that surficial recharging water and groundwater water table were quickly connected in the system. When relating satellite macro-classes to head measurements, no Class 1 was observed during the same time period, and very sporadically Class 2 was detected. In contrast, Class 3 and especially Class 4 dominated the time series, suggesting that the water in the basin was rare or not present in the system during this time frame. Given the saturated hydraulic conductivity of the topsoil as $Ks = 2.5 \times 10^{-4}$ m/s (Masetti et al., 2016), we calculated that the total volume of water stored in the basin completely infiltrated through the bottom surface in less than 4 days from the last rainfall event. This result is confirmed by satellite monitoring indicating that all images taken four, or more, days before the last antecedent rainfall event show the ARB empty (Stage 1 in Fig. 4).

In the 2013 period (Fig. 5 – mid panel), the correlation between recharge and satellite information was again evident. Before March 2013, limited groundwater head response was found and Class 4 was the only one in this period. From April 2013 on, the rainfall events became progressively more intense and frequent, respect to 2012 with more than 240 mm in one month. At the beginning of the period, there was a dramatic head response, with fluctuation of $\Delta h > 10$ m with regards to the basal head level. The following satellite images highlight a period of complete presence of water in the ARB detected by the satellites (Class 1). After June 2013, water in the ARB progressively decreased, a behavior closely followed by the decrease in groundwater depths toward the basal values. In this time phase, the basin was in the Class-1 condition even after 12 days from the last antecedent rainfall event, consistent with the infiltration capacity of the ARB somewhat diminished in 2013 due to incipient formation of clogging (Stage 2 in Fig. 4).

In the beginning of August 2013, the ARB started to be found always empty (Class 4) less than 3 days before the last antecedent rainfall event. This condition is maintained till the end of the year even under a short intense rainfall event such as the one of late November 2013 when a change of depth to groundwater $\Delta h \approx 2$ m was observed (Fig. 5 – mid panel). The six months, from late June to late December 2013, recorded a small amount of total rainfall of about 390 mm, with more than 80 mm in the seven-day long event in late November. This prevailing situation of Class 4 condition indicates the return of good infiltration characteristics of ARB topsoil (Stage 3 in Fig. 4).

A new high recharge event was observed at the end of December 2013, correlating well with the Class 1 status of the system. However, this appeared to be the last recharge-satellite correlated event from the analyzed time series. For all recharge event in 2014 (Fig. 5 – bottom panel), the satellite persistently revealed the same information: All events were corresponding to Class 1 status of the ARB, indicating that the ARB was completely clogged even 20 days before the last antecedent rainfall event (Stage 4 in Fig. 4). This mean that, despite being full, the ARB was no longer influencing the aquifer due to limited infiltration through the ARB topsoil. This condition was related to a total rainfall amount of 323 mm occurred in one month, between mid December 2013 and mid January 2014.

Summarizing the evolution of the recharge events from 2012 to 2014 behavior and their correlation with the satellite information, the progressive impact of clogging on the ARB and the reduced infiltration capacity of the topsoil were evident. The analysis of recharge events in 2013 confirmed the hypothesis that the system was transitioning from unclogged to clogged ARB topsoil conditions.

The reason of this transitioning between unclogged to clogged conditions can be explained recalling that, in the analyzed ARB basin, clogging is mostly associated to biological activities (mainly biofilm) rather than other type of clogging, such as physical or chemical clogging (Masetti et al., 2016). When exposed to air (i.e. during the period when the ARB display $p \rightarrow 0$) recently-formed biofilm can be subject to rapid biodegradation and removal due to wind action or arrival of the successive water in the basin washing away the dead biological matter (e.g. Martin, 2013). Indeed, the basin has been observed almost dry in many satellite images during 2012 and most of 2013, resulting in a longer exposure of the biofilm to conditions adverse to its growth and stabilization. The last storm water event in 2013 could have accelerated the formation of the bio-clogging, favored also by the absence in 2014 of extended dry period, potentially favoring biofilm degradation and by a progressive reduction of the infiltration capacity of the topsoil compared to that in the initial part of 2013. Note that the progressive reduction in infiltration rates were not due to the implication of watertable rising towards the basin surface (i.e. groundwater mounding). Indeed, the groundwater depth was always higher than 20 m during all the monitoring period (Fig. 5), including during the heaviest rainfall or storm water events.

The results are summarized in Fig. 6, which clearly highlights how the four Stages have specific correlation with image classes and ground measurements. For each satellite image, Fig. 6 relates the four Classes of water coverage in the ARB (Section 2.3.3) with: (a) the measured groundwater depth (GW depth) and (b) a variable representing the days passed from the date of image acquisition to the last rainfall event occurred before the image (LRBI). Data are grouped by the four Stages of clogged/unclogged conditions described at the beginning of this section. Each box reports the mean and standard deviation of groundwater depth and a density ellipse with a 90% coverage, where data are more than two. The distinction between the unclogged conditions (Stages 1 and 3) and the clogged conditions (Stages 2 and 4) is rather clear. It confirms that Stage 1 and 3 are characterized by a prevalence of Class 4 images (no water in the ARB) and high groundwater depth values, related to period with low rainfall. On the contrary, Stages 2 and 4 are characterized by a prevalence of Class 1 and 2 images (ARB full or almost full of water) and low groundwater depth values, related to period with high rainfall.

3.2. Exploratory modeling analysis

To provide a quantitative estimate of the change in infiltration rate in the basin due to the impact of clogging on the ARB, we performed new simulation using the numerical model described by Masetti et al. (2016). The model was designed to replicate the relationship between groundwater head changes in the local aquifer nearby the ARB and local rainfall events under variable topsoil conditions. The setup, described in detail in the Supplementary Material, is based on a finite element solution of unsaturated flow with transient boundary conditions. The model was calibrated and verified under transient conditions over different time lengths (weeks or months, according to the number of successive rainfall events to be analyzed), and it is considered sufficiently adequate for the hydraulic assessment of the aquifer-ARB relationship.

This work extends the use of the validated model as a powerful exploratory tool for a quantitative assessment of Stages 2, 3 and 4, identified by the correlation between satellite image classes and ground measurements (Section 3.1) occurred in the 2013–2014 period, where the ARB had different phases of unclogged and clogged conditions (Supplementary material, Fig. 1S). We modify the model properties to account for the evolution of biofilm development on the basin surface. To ensure that the modification would not affect the accuracy of the solution, the model was validated against a new dataset based on observed groundwater head measurement in PZ3, which was the piezometer influenced by the artificial recharge from the ARB (Supplementary Material, Fig. 2S). The flooded ARB surface is simulated as a transient ponding condition to represent the presence of water in the basin during the period of 100% surface covered by water. Stage 2. First temporary clogging process (March-May 2013).

In this Stage, we observed a continuous decrease of the groundwater head in the aquifer in PZ3 when the basin continued maintaining water within its boundaries, from May to July 2013. To match this observation in the numerical model, we adopt an effective hydraulic approach based on transient exponential reduction of the

saturated hydraulic conductivity (K_s) (e.g., Pedretti et al., 2012b) on the elements in the model representing the ARB topsoils, as stepped decay K_s function. The calibrated model resulted in a progressive reduction of the topsoil K_s over time from the initial $K_s = 2.5 \times 10^{-4}$ m/s (the value associated to unclogged topsoil conditions) to $K_s = 1.6 \times 10^{-6}$ m/s. The newly estimated value, about two orders of magnitude lower than the initial hydraulic conductivity, indicates very rapid clogging processes in the site, remarkably affecting the topsoil conditions. Indeed, $K_s = 2.5 \times 10^{-4}$ m/s is closer to typical hydraulic conductivity values of clean mid-coarse sands, characterizing the local aquifer, while $K_s = 1.6 \times 10^{-6}$ m/s represents a value more typical of fine sands, suggesting that the topsoil may effectively behave as a finer grained unconsolidated soil from a hydrogeological perspective due to the incipient effects of bioclogging.

Stage 3. The self-declogging condition associated with the biodegradation of the clogging (June-August 2013). For this Stage, the model is fitted with a hydraulic conductivity of $K_s = 1 \times 10^{-4}$ m/s, which is almost equal to the initial one, showing the restoration of a high infiltration condition in the ARB topsoil. This is consistent with our conceptual model, which suggests that bio-clogging may have been removed from the topsoil after the biodegradation process during the time periods without presence of water in the ARB detected by the satellites images.

Stage 4. The formation of persistent clogging (December 2013January 2014).

In Stage 4, we had to lower substantially the topsoil hydraulic efficiency. The model started to match the observed groundwater depth changes in PZ3 when $K_s = 3.4 \times 10^{-7}$ m/s, about three orders of magnitude lower than the original "unclogged" value. Such a low K_s highlights the more extensive clogging conditions taking place at the end of 2013, given that such low hydraulic conductivity is typical of poorly permeable soils, such as silty soils. Note that an even lower value than $K_s = 3.4 \times 10^{-7}$ m/s may actually characterize the topsoil during the end of 2013. Indeed, any lower K_s can minimize the infiltration from the ARB topsoil, rendering the system effectively impermeable. Thus, the actual value may be lower than $K_s = 3.4 \times 10^{-7}$ m/s, and we use this estimate amount only as a "reference" hydraulic conductivity required for the system to become "impermeable".

The correlation between satellite images and ground measurements discussed in Section 3.1. allows to use the numerical model to infer new quantitative interpretations on ARB management and bioclogging formation, enabled by the satellite monitoring: (a) the reproduction of the transient first bioclogging phase though the implementation of a "time dependent" hydraulic conductivity function; (b) the verification of the self-declogging phase, by giving a precise quantitative estimation of the self restored high hydraulic conductivity of the ARB bottom; (c) proving the fast rate of bioclogging formation by evaluating the three orders of magnitude decay of hydraulic conductivity values occurred in two months, and the reference hydraulic conductivity value for which recharge through the ARB becomes negligible.

4. Conclusion

The use of artificial recharge basins (ARBs) is a practical solution to cope with flooding problem while maintaining adequate aquifer recharge under an increasing impermeable area due to urbanization, especially near a major metropolis like Milan. In large basins (such as the 22 ha one analyzed in this work), a common problem is to develop ground-based monitoring scheme to obtain reliable data time series of water level within the ARB. These data are important to closely track the basin status and to understand its specific hydrological evolution in terms of infiltration efficiency.

Frequent remote sensing of the ARB surface is found crucial to monitor the basin performance for support decision makers to pro-actively prevent or alleviate hazardous conditions. The multi-temporal images from the COSMO-SkyMed constellation offer a suitable tool to investigate and verify the capability for surface water observations that closely characterize hydrological features and processes occurred in the basin. Moreover, combinations of such space-borne X-band SAR systems, such as CSK, TanDEM-X (DLR, 2018), and the future LOTUSat-1, 2 (2018), can contribute to significant and practical advances for environmental monitoring capable of capturing the dynamics of hydrological processes impacted by the increasing urbanization trend across the world.
The following specific conclusions were drawn from this study:

(1) Transient satellite analysis can be efficiently used in combination with ground monitoring and numerical modeling to estimate the total infiltration capacity of the ARB, and in particular to estimate the relative change in hydraulic conductivity of the ARB topsoil when transitioning from unclogged to clogged conditions, in order to evaluate the degree of clogging formation in the ARB;
(2) Using appropriate remote sensing information within hydrogeological models can greatly help the exploratory power of models by improving the assessment of the impact on the local aquifer recharge boundary conditions from the targeted ARB. The CSK SAR constellation is demonstrated to be suitable for this task, owing to frequent acquisitions on the Lonate-Pozzolo basin with the SAR system properties that are appropriate to ARB surface water monitoring (e.g., high spatial resolution, high signal-to-noise ratio, and surface imaging capability regardless of cloud and darkness).
(3) Biofilm can rapidly develop when sequential rainfall events are separated by only few dry days, limiting the exposed to air and consequently the natural self-degradation of the biofilm. If biofilm keeps developing, the hydraulic conductivity of the basin surface can rapidly decrease by more than three orders of magnitude, completely altering the relationship with the local groundwater regime. Thus, the most important factor related to rainfall that affects clogging formation is not represented by the average annual rainfall but by the occurrence of extended wet periods, even if they cover a limited part of the year;
(4) Quantitative estimation of the evolution of the infiltration rate provides useful insights into the general recharge behavior of basins that can be used to make reliable economical plans in both the design and monitoring phase.

Acknowledgments

This project was carried out using CSK® Products © ASI (Italian Space Agency), delivered under an ASI licence for use within the framework of the COSMO-SkyMed Open Call for Science (Project ID 00015/8/252/1014). The research carried out at the Jet Propulsion Laboratory, California Institute of Technology, related to hydrological impacts within and beyond urban areas, was supported by the National Aeronautics and Space Administration (NASA) Land-Cover and LandUse Change (LCLUC) Program.

The authors acknowledge the comments and criticisms by the Editors and Reviewers, who helped to improve the quality of this article.

Appendix A. Supplementary material

Supplementary data to this article can be found online at https:// doi.org/10.1016/j.jhydrol.2018.09.067.

References

Agenzia Spaziale Italiana (ASI). COSMO-SkyMed SAR Products Handbook, 2007 [Online]. Available: http://www.cosmo-skymed.it/docs/ASICSM-ENG-RS-092-ACSKSARProductsHandbook.pdf.

Alsdorf, D.E., Rodríguez, E., Lettenmaier, D.P., 2007. Measuring surface water from space. Rev. Geophys. 45, RG2002.

Bamler, R., 1999. The SRTM Mission: A World Wide 30m Resolution DEM from SAR Interferometry in 11 Days. Photogrammetric Week, Wichmann.

Bartsch, A., Trofaier, A.M., Hayman, G., Sabel, D., Schlaffer, S., Clark, D.B., Blyth, E., 2012. Detection of open water dynamics with ENVISAT ASAR in support of land surface modelling at high latitudes. Biogeosciences 9, 703–714.

Boni, G., et al., 2016. A prototype system for flood monitoring based on flood forecast combined with COSMO-SkyMed and Sentinel-1 data. IEEE J. Select. Top. Appl. Earth Observ. Remote Sens. 9 (6), 2794–2805.

Bouwer, H., 2002. Artificial recharge of groundwater: hydrogeology and engineering. Hydrogeol. J. 10 (1), 121–142.

Brakenridge, G.R., Nghiem, S.V., Anderson, E., Chien, S., 2005. Space-based measurement of river runoff. Eos Trans. AGU 86 (19), 185–188.

Brakenridge, G.R., Nghiem, S.V., Anderson, E., Mic, R., 2007. Orbital microwave measurement of river discharge and ice status. Water Resour. Res. 43.

Buhyain, C., 2015. An approach towards site selection for water banking in unconfined aquifers through artificial recharge. J. Hydrol. 523, 465–474.

Canadian Space Agency, 2017. http://www.asc-csa.gc.ca/eng/satellites/radarsat2/ Default.asp (web access, Dec 2017).

Coelho, V.H., Montenegro, S., Almeida, C.N., Silva, B.B., Oliveira, L.M., Gusmão, A.V., Freitas, E.S., Montenegro, A.A., 2017. Alluvial groundwater recharge estimation in semi-arid environment using remotely sensed data. J. Hydrol. 548, 1–15.

Coletta, A., Valentini, G., Capuzi, A., Caltagirone, F., De Carlo, M., De Luca, G.F., Battazza, F., Covello, F., 2008. The COSMO-SkyMed program: description of mission system and first results. Rivista Italiana di telerilevamento 40, 5–13 (in Italian).

e geos, COSMO-SkyMed Image Calibration, 2012. Available: http://www.egeos.it/ products/pdf/COSMO-SkyMed-Image_Calibration.pdf.

DFO, Dartmouth Flood Observatory, 2016. http://floodobservatory.colorado.edu/, (accessed 15 Jun. 2017).

Ding, X., Nunziata, F., Li, X., Migliaccio, M., 2015. Performance analysis and validation of waterline extraction approaches using single- and dual-polarimetric SAR data. IEEE J. Select. Top. Appl. Earth Observ. Remote Sens. 8 (3), 1019–1027.

DLR, 2018. TanDEM-X – the Earth in three dimensions. URL: http://www.dlr.de/dlr/en/ desktopdefault.aspx/tabid-10378/566_read-426/#/gallery/345, (accessed May 2018).

ESA, 2017. https://earth.esa.int/web/sentinel/user-guides/sentinel-2-msi/resolutions/ spatial.

ESA, 2017. http://www.esa.int/Our_Activities/Observing_the_Earth/Copernicus/ Sentinel-1.

Grieco, G., Nirchio, F., Migliaccio, M., 2015. Application of state-of-the-art SAR X-band geophysical model functions (GMFs) for sea surface wind (SSW) speed retrieval to a data set of the Italian satellite mission COSMO-SkyMed. Int. J. Remote Sens. 36 (9), 2296–2312.

Grimani, V., Bussi, B., Salemme, P., Perrera, A., Pepe, P., Inversi, P., Esposito, P.G., Oddone, A., De Luca, G.F., Coletta, A., 2016. CSK mission status and experimentation results. In: Proceedings of EUSAR 2016: 11th European Conference on Synthetic Aperture Radar, Hamburg, Germany, pp. 1–3.URL: http://ieeexplore.ieee.org/stamp/stamp.jsp?tp=&arnumber=7559443&isnumber=7559230.

Hostache, R., Matgen, P., Schumann, G., Puech, C., Hoffmann, L., Pfister, L., 2009. Water level estimation and reduction of hydraulic model calibration uncertainties using satellite SAR images of floods. IEEE Trans. Geosci. Remote Sens. 47 (2), 431–441.

Houle, J., Roseen, R., Ballestero, T., Puls, T., Sherrard, J., 2013. Comparison of maintenance cost, labor demands, and system performance for LID and conventional stormwater management. J. Environ. Eng. 139, 932–938.

JV-LOTUSat 1,2, 2018. URL: http://space.skyrocket.de/doc_sdat/jv-lotusat-1.htm, (accessed May 2018).

Kattan, Z., Kadkoy, N., Nasser, S., Safadi, M., Hamed, A., 2010. Isotopes and geochemistry in a managed aquifer recharge scheme: a case study of fresh water injection at the Damascus University Campus. Syria. Hydrol. Process. 24, 1791–1805.

Khalaf, A., Donoghue, D., 2012. Estimating recharge distribution using remote sensing: a case study from the West Bank. J. Hydrol. 414–415, 354–363.

Li, X.-M., Lehner, S., 2014. Algorithm for sea surface wind retrieval from TerraSAR-X and TanDEM-X data. IEEE Trans. Geosci. Remote Sens. 52 (5), 2928–2939.

Martin, R. (Ed.), 2013. Clogging Issues Associated with Managed Aquifer Recharge Methods. IAH Commission on Managing Aquifer Recharge, Australia.

Masetti, M., Nghiem, S.V., Sorichetta, A., Stevenazzi, S., Fabbri, P., Pola, M., Filippini, M., Brakenridge, G.R., 2015. Urbanization affects air and water in Italy's Po plain. EOS 96 (21), 13–16.

Masetti, M., Pedretti, D., Sorichetta, A., Stevenazzi, S., Bacci, F., 2016. Impact of a stormwater infiltration basin on the recharge dynamics in a highly permeable aquifer. Water Resour. Manage. 30 (1), 149–165.

Nghiem, S.V., Li, F.K., Neumann, G., 1997. The dependence of ocean backscatter at Kuband on oceanic and atmospheric parameters. IEEE Trans. Geosci. Remote Sens. 35 (3), 581–600.

Nghiem, S.V., Leshkevich, G.A., Stiles, B.W., 2004. Wind fields over the great lakes measured by the SeaWinds Scatterometer on the QuikSCAT satellite. J. Great Lakes Res. 30 (1), 148–165.

Nghiem, S.V., Wardlow, D.B., Allured, D., Svoboda, M.D., LeComte, D., Rosencrans, M., Chan, K.S., Neumann, G., 2012. Microwave remote sensing of soil moisture – science and applications, Chapter 9, Part III, pp. 197–226. Remote Sensing of Drought – Innovative Monitoring Approaches, Drought and Water Crises Book Series. CRC Press, Taylor and Francis ISBN 978-1-4398-3557-9.

Nghiem, S.V., Zuffada, C., Shah, R., Chew, C., Lowe, S.T., Mannucci, A.J., Cardellach, E., Brakenridge, G.R., Geller, G., Rosenqvist, A., 2017. Wetland monitoring with Global Navigation Satellite System reflectometry. Earth Space Sci. 4, 16–39. https://doi.org/ 10.1002/2016EA000194.

Paloscia, S., Pampaloni, P., Pettinato, S., Santi, E., 2008. A comparison of algorithms for retrieving soil moisture from ENVISAT/ASAR images. IEEE Trans. Geosci. Remote Sens. 46 (10, Part 2), 3274–3284. https://doi.org/10.1109/TGRS.2008.920370.S. Digital Object Identifier.

Paloscia, S Pettinato, Santi, E., 2012. Combining L and X band SAR data for estimating biomass and soil moisture of agricultural fields. Eur. J. Remote Sens. 45, 99–109. https://doi.org/10.5721/EuJRS20124510.

Pedretti, D., Fernàndez-Garcia, D., Sanchez-Vila, X., Barahona-Palomo, M., Bolster, D., 2011. Combining physical-based models and satellite images for the spatio-temporal assessment of soil infiltration capacity. Stoch. Environ. Res. Risk Assess. 25, 1065.

Pedretti, D., Barahona-Palomo, M., Bolster, D., Fernàndez-Garcia, D., Sanchez-Vila, X., Tartakovsky, D.M., 2012a. Probabilistic analysis of maintenance and operation of artificial recharge ponds. Adv. Water Resour. 36, 23–35.

Pedretti, D., Barahona-Palomo, M., Bolster, D., Sanchez-Vila, X., Fernàndez-Garcia, D., 2012b. A quick and inexpensive method to quantify spatially variable infiltration capacity for artificial recharge ponds using photographic images. J. Hydrol. 430–431, 118–126.

Pettinato, S., Santi, E., Brogioni, M., Paloscia, S., Palchetti, E., Xiong, C., 2013. The potential of COSMO-SkyMed SAR images in monitoring snow cover characteristics. Geosci. Remote Sens. Lett. IEEE 10 (1), 9–13. https://doi.org/10.1109/LGRS.2012. 2189752.

Pettinato, S., Santi, E., Paloscia, S., Aiazzi, B., Baronti, S., Garzelli, A., 2014. Snow cover area identification by using a change detection method applied to COSMO-SkyMed images. J. Appl. Remote Sens. 8 (1), 084684. https://doi.org/10.1117/1.JRS.8. 084684.

Pierdicca, N., Chini, M., Pulvirenti, L., Candela, L., Ferrazzoli, P., Guerriero, L., Boni, G., Siccardi, F., Castelli, F., 2009. Using COSMO-SkyMed data for flood mapping: Some case-studies. In: 2009 IEEE International Geoscience and Remote Sensing Symposium, Cape Town, pp. II-933-II-936. http://doi.org/10.1109/IGARSS.2009. 5418251.

Pradhan, B., Tehrany, M.S., Jebur, M.N., 2016. A new semiautomated detection mapping of flood extent from TerraSAR-X satellite image using rule-based classification and taguchi optimization techniques. IEEE Trans. Geosci. Remote Sens. 54 (7), 4331–4342.

Pulvirenti, L., Marzano, F.S., Pierdicca, N., Mori, S., Chini, M., 2014. Discrimination of water surfaces, heavy rainfall, and wet snow using COSMO-SkyMed observations of severe weather events. IEEE Trans. Geosci. Remote Sens. 52 (2), 858–869.

Pulvirenti, L., Chini, M., Pierdicca, N., Boni, G., 2016. Use of SAR data for detecting floodwater in urban and agricultural areas: the role of the interferometric coherence. IEEE Trans. Geosci. Remote Sens. 54 (3), 1532–1544.

Racz, A.J., Fisher, A.T., Schmidt, C.M., Lockwood, B.S., Los Huertos, M., 2012. Spatial and temporal infiltration dynamics during managed aquifer recharge. Ground Water 50 (4), 562–570.

Ran, L., Lu, X.X., 2012. Delineation of reservoirs using remote sensing and their storage estimate: an example of the Yellow River basin, China. Hydrol. Process. 26, 1215–1229.

Santoro, M., Wegmüller, U., 2014. Multi-temporal synthetic aperture radar metrics applied to map open water bodies. IEEE J. Select. Top. Appl. Earth Observ. Remote Sens. 7 (8), 3225–3238.

Shi, Y.M., Feng, L., Gong, J.Y., 2017. Four decades of the morphological dynamics of the lakes in the Jianghan Plain using Landsat observations. Water Environ. J. 31–3, 353–359.

Torre A., Calabrese D. Porfilio M., 2011. COSMO-SkyMed: Image quality achievements. In: Recent Advances in Space Technologies (RAST), 5th International Conference on, Istanbul, 2011, pp. 861–864.
Ulaby, F.T., Moore, R.K., Fung, A.K., 1986. Microwave remote sensing: active and passive. Surface Scattering and Emission Theory, vol. III.
United Nations, Committee on the peaceful uses of outer space, 2017. Thematic priority 5. Strengthened Space Cooperation for Global Health. UN Report A/ac.105/1172.
Xie, L., Hong, Z., Chao, W., Fulong, C., 2016. Water-Body types identification in urban areas from radarsat-2 fully polarimetric SAR data. Int. J. Appl. Earth Observ. Geoinf. 50, 10–25.

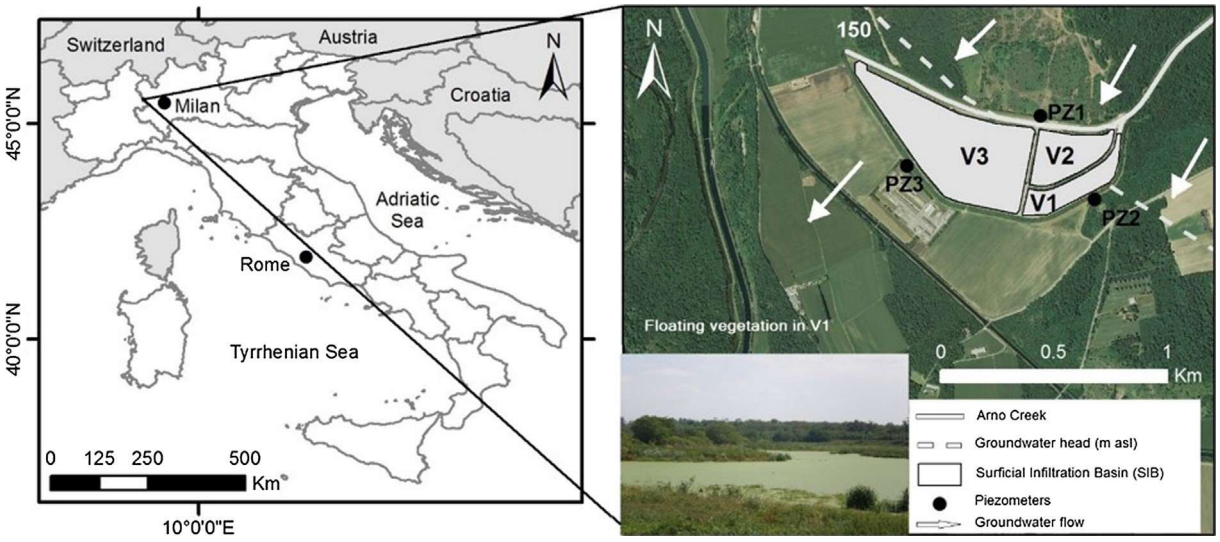

Fig. 1. Location of the study area and detail of the sub-basins composing the superficial infiltration basin, the inset photograph shows the floating vegetation on the water surface. Hydrogeological sketch of the area with the position of the basin (bottom panel) (adapted from Masetti et al., 2016).

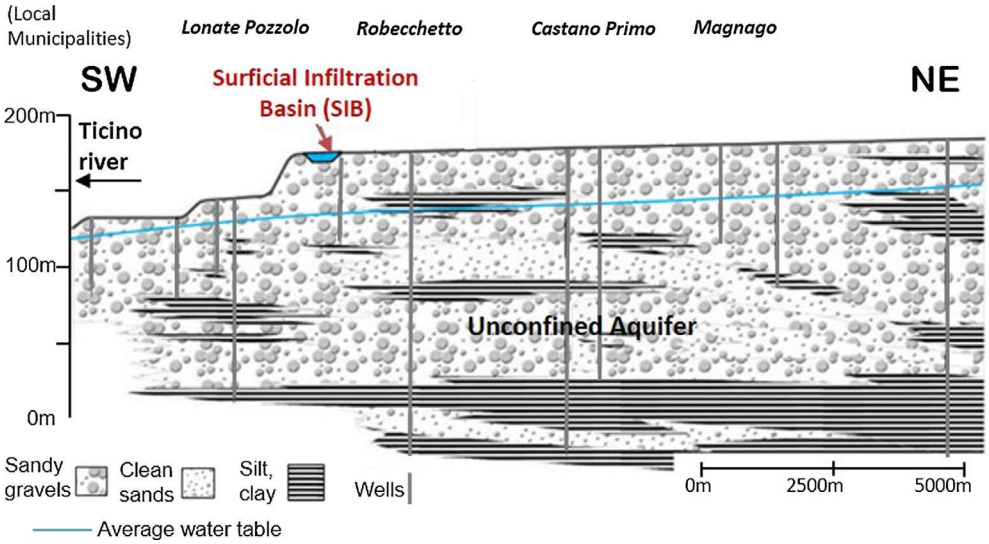

Fig. 2. Hydrogeological sketch of the area with the position of the SIB.

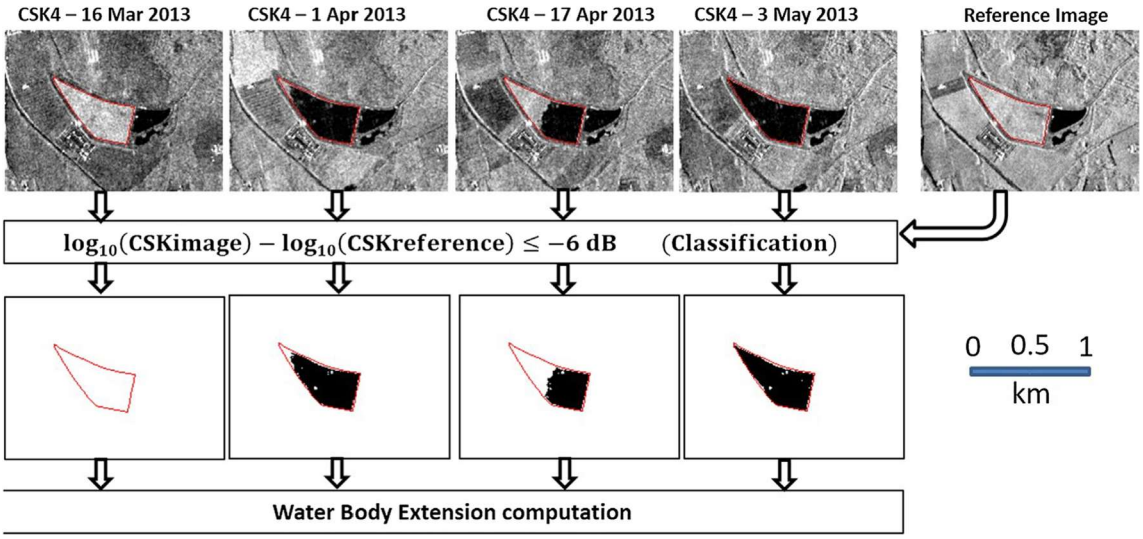

Fig. 3. CSK images acquired on different days and classified water body in black color, respect to reference image. The red line indicates the boundary of V3 pool of the basin. V1 and V2 were excluded from this analysis, as explained in the text, and were blackened out in right panel. (For interpretation of the references to color in this figure legend, the reader is referred to the web version of this article.)

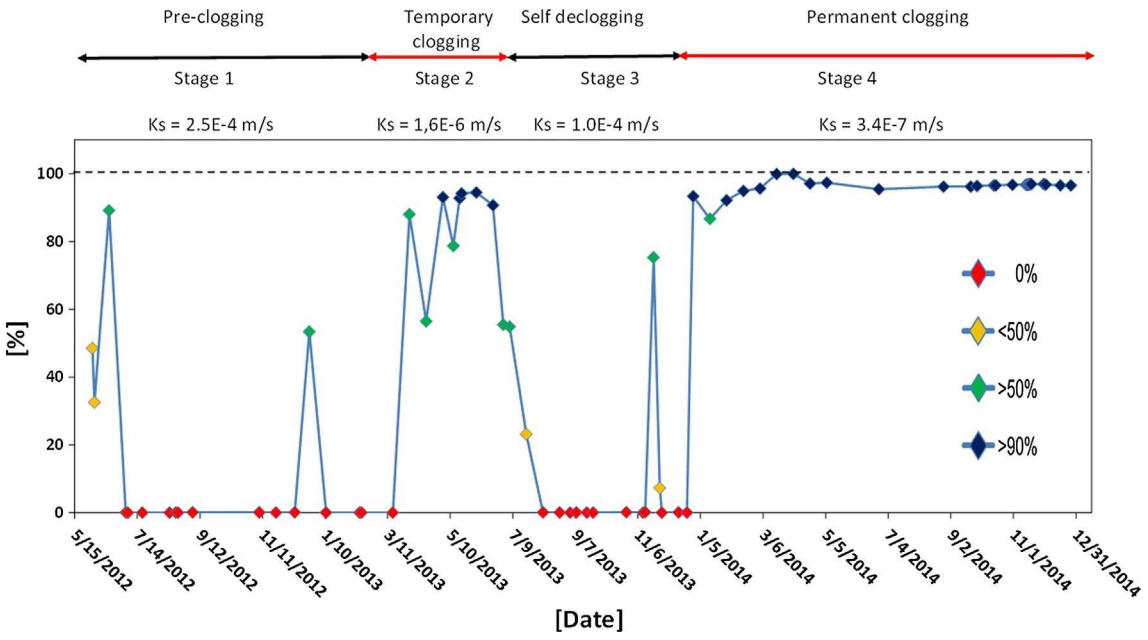

Fig. 4. Water body surface estimated from CSK satellite passes. The 100% represents the V3 pool completely filled. Ks indicated the equivalent hydraulic conductivity of topsoil under different Stage of clogging conditions.

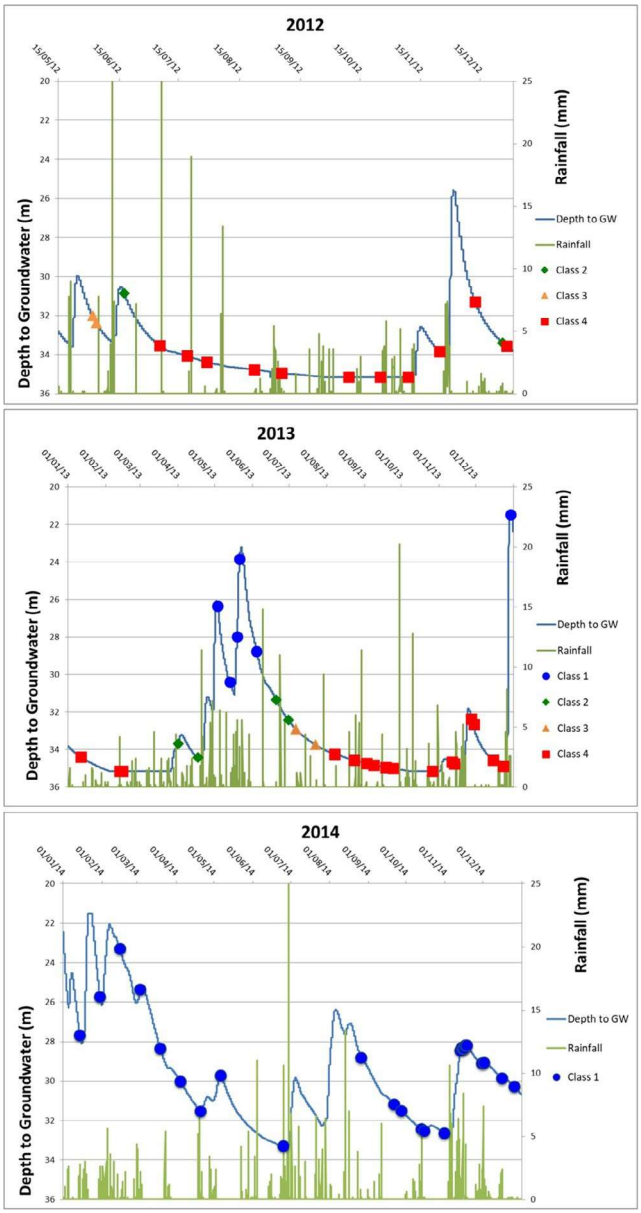

Fig. 5. GW depth and rainfall (measured every hour) in years 2012 (top panel), 2013 (mid panel) and 2014 (bottom panel). Points on GW head lines indicate the Classes of basin surface covered by water. Data refers to PZ3.

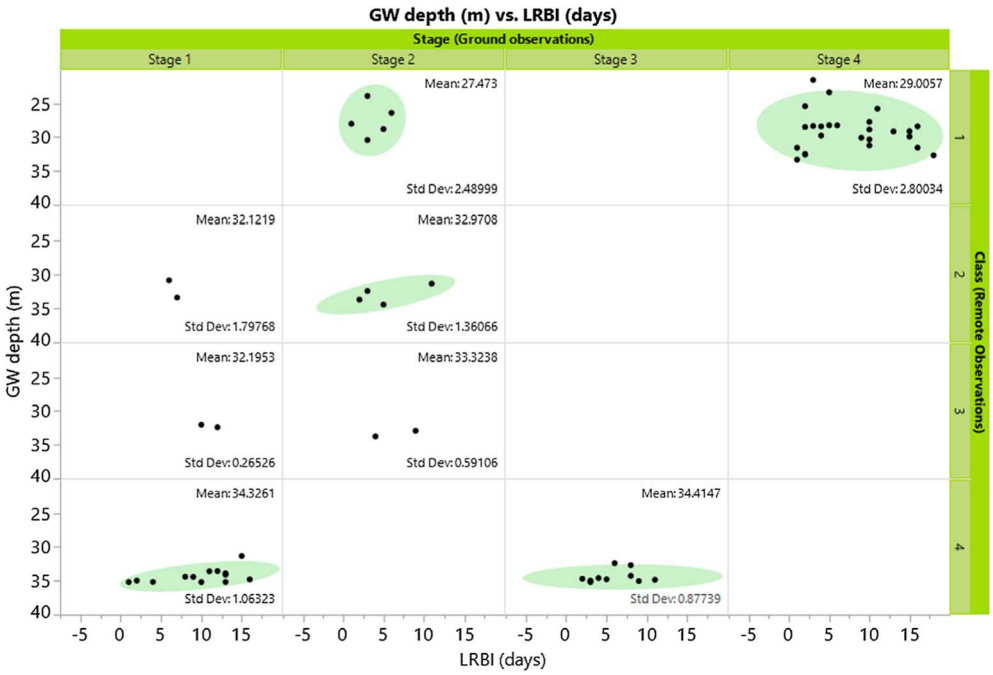

Fig. 6. Multi-variables plot relating groundwater depth (GW depth in m) to the days passed from the date of image acquisition to the last rainfall event occurred before the image (LRBI) for each combination of Stages (unclogged/clogged conditions) and Classes (water presence in the ARB).